PAPER

3D measurement method for LAMOST fiber end-faces under front and back illumination

IOP Publishing Measurement Science and Technology
Meas. Sci. Technol. **36** (2025) 065004 (14pp) https://doi.org/10.1088/1361-6501/add60f

3D measurement method for LAMOST fiber end-faces under front and back illumination

Rui Wang, Shijie Li, Jiawen Xin, Jian Zhou and Junhua Sun*

School of Instrumentation and Optoelectronic Engineering, Beihang University, Beijing 100191, People's Republic of China

E-mail: Sjh@buaa.edu.cn

Received 20 November 2024, revised 8 April 2025
Accepted for publication 8 May 2025
Published 22 May 2025

Abstract

In the Large Sky Area Multi-Object Fiber Spectroscopic Telescope (LAMOST) project, fiber positioners align the fiber ends to designated positions on the focal plane to capture high-quality spectra of specific celestial objects. Therefore precise measurement of fiber end positions is essential for accurate control in the closed-loop positioning system. Current measurement systems primarily rely on 2D planar methods, which cannot achieve precise positioning of fiber ends on LAMOST's curved focal plane. However traditional 3D measurement methods often struggle to reconstruct specific targets, leading to excessive data redundancy and reduced accuracy. To address these issues, this paper proposes a novel monocular vision-based 3D measurement method for LAMOST fiber ends under both front and back illumination. In this method, coding points and a baseline ruler are placed on the focal plane; the coding points help determine camera poses, while the baseline ruler recovers the physical scale of the measurement results. Images of the coding points and fiber end-faces are first captured under front and back illumination using a single camera that takes frames with movement, and the enhanced spot-grayscale distribution model algorithm is introduced as an efficient and accurate method for spot center extraction. Subsequently, the decoding method of coding points-clustering and pattern matching method is proposed for automated recognition and decoding of the coding points. Finally, a fusion-coded structure-from-motion based 3D reconstruction method, is employed to measure the fiber end positions in 3D. Results show that the method achieves a root mean square error of 0.049 mm in fiber optic 3D measurement error. The proposed 3D measurement method for fiber ends is vital for closed-loop control in LAMOST and is also applicable to high-precision measurement of the fiber ends in other multi-object spectroscopic telescopes.

Keywords: 3D measurement, spot center extraction, structure from motion

1. Introduction

Astronomical spectra contain critical physical information, making precise acquisition and analysis essential. Advances in modern astronomy and space technology have enabled large-scale sky surveys through the development of 'multi-target spectral fiber' technology. The Chinese Large Sky Area Multi-Object Fiber Spectroscopic Telescope (LAMOST) telescope (Cui *et al* 2012), with its large number of fibers arranged on a curved focal plane, boasts an ultra-large aperture and wide field of view, securing a leading position in global sky survey projects. These features allow LAMOST to efficiently conduct

* Author to whom any correspondence should be addressed.

large-scale astronomical observations. To maximize the accuracy of spectral information acquired by LAMOST, each fiber end on the curved focal plane must be precisely aligned with its corresponding star. However, fiber positioning errors are inevitable due to factors like machining precision, motor operation accuracy, and focal plane installation accuracy. Accurate measurement of fiber end positions on the curved focal plane is a prerequisite for developing the LAMOST closed-loop fiber positioning system (Xing *et al* 2007) and ensuring high-precision fiber positioning.

Multi-target spectral telescopes like LAMOST are employed worldwide. Examples include the prime focus spectrograph (PFS) on Japan's Subaru Telescope (Fisher *et al* 2014), the dark energy spectrograph (DES) in the United States, and the multi-object optics and near-infrared spectrograph (MOONS) in the UK (Montgomery *et al* 2016). Multi-target spectral telescope features multiple optical fibers arranged on the focal plane. Each fiber can be individually aligned with a target, transmitting its optical signals to the spectrometer for analysis. Consequently, these telescopes require a sophisticated fiber-optic positioning system to precisely adjust the fiber end face, capturing spectral information through closed-loop feedback control.

Various countries have proposed different approaches to achieve precise fiber positioning. The Subaru Telescope in Japan developed a photometric camera (Wang *et al* 2012) for its new multi-fiber spectrometer to measure the two-dimensional position of the fiber end face and provide feedback for COBRA system positioning. The photometric camera captures images of backlit fiber end face on the focal plane, measures them in two dimensions within the COBRA system's coordinate system, and converts these positions to the 2D coordinates of the fibers on the focal plane. In the DESI telescope in the USA, to ensure closed-loop control during fiber positioning, the fiber is back illuminated after each movement, and its actual 2D position is measured by a on-axial CCD camera located in the central aperture of the primary mirror (Schubnell *et al* 2016). The deviation between the actual and set 2D positions of the fiber, as measured by the CCD camera, is sent to the fiber positioning controller, which adjusts the fiber's position for precise correction. The European 4MOST telescope's metering system (Winkler *et al* 2016, 2022) comprises four identical metrological cameras that capture images of the measurement and fiducial fibers. After capturing fiber images, a computer program in the metering system extracts the profiles of all fibers, calculates the center of mass for each, and determines the 2D positions of all measurement fibers relative to the fiducial fiber on the focal plane through coordinate system transformation. MOONS is the third-generation visible and near-infrared spectrograph for the ESO Very Large Telescope (Watson *et al* 2022). The MOONS fiber-optic unit is positioned at the end of each axis with a reference point identifiable by the fiber-optic measurement camera. A high-resolution camera captures images of the fiber-optic positioning unit under ambient light, determines its biaxial orientation from the reference point in the image, and then measures the fiber's 2D position using backlight illumination.

In LAMOST system, the initial fiber-optic positioning system (Li *et al* 2004) uses an open-loop design, with its performance calibrated annually through short-range testing. However, the open-loop system provides low positioning accuracy and the annual calibration interval is too long, resulting in gradual accuracy degradation and difficulty in achieving high-precision positioning. To enhance the accuracy of the fiber-optic positioning system and reduce the need for frequent calibration, upgrading to a closed-loop system is essential. Precise optical fiber position detection is critical to the closed-loop feedback mechanism and the overall performance of the fiber-optic positioning system (Xing *et al* 2007). Therefore Gu *et al* (2008) developed a fiber-optic 2D position detection system utilizing a triple line array CCD. The system employs image stitching within a face-array camera partitioning scheme to divide a large field of view into multiple sub-regions. These sub-regions are captured by moving or rotating a single face-array camera and are subsequently stitched together. Later, Zhao *et al* (2018) employed a polynomial calibration method to optimize the 2D coordinates of the fibers on the focal plane. This method simplifies the mapping between image points and spatial points, enabling the planar coordinates of spatial points to be deduced from image points through a fitting formula. Pan (2022) installed a visual measurement system, comprising a high-resolution CMOS camera and a telephoto lens, around the MB primary mirror, approximately 20 meters from the focal plane, to zone the optical fibers. The camera was positioned off the telescope's optical axis to avoid obstructing the optical path, preventing an angle between the focal plane of the fibers and the camera's imaging plane, thereby reducing measurement errors.

In practice, the focal plane of LAMOST is curved. In practice, the focal plane of LAMOST is curved. The focal plane exhibits a spherical curvature, with a total bending angle of approximately 2.88 ° over the entire focal plane. However, most existing optical fiber end face measurement systems employ a two-dimensional planar method. The current LAMOST fiber end face position is measured using a two-dimensional image method based on multi-camera splicing. The cameras are positioned far apart to approximate the curved surface as a flat plane, which will introduce a maximum measurement error of 1.69 mm. This error may affect the positioning accuracy of the fibers and should be considered in high-precision measurements. Therefore, it is essential to study high-precision 3D measurement of the LAMOST fiber end face position.

This study presents an innovative 3D measurement method that overcomes key challenges in optical metrology for astronomical instrumentation. Initially developed for the LAMOST telescope upgrade, our approach significantly improves the high-precision measurement of micrometer-scale fiber targets on curved surfaces, a persistent challenge in metrology. By integrating front and back illumination with enhanced spot center extraction grayscale distribution model (ES-GDM) and fusion-coded structure-from-motion (SfM), we achieve unprecedented precision in fiber end-face measurements, reducing root mean square error (RMSE) by 34.7% compared to

conventional methods. Beyond astronomy, this work establishes a new paradigm for contactless 3D measurement of small features, attaining measurement error of 0.049 mm while improving computational efficiency by 5.89× over traditional SfM. These advancements are particularly valuable for industrial metrology, biomedical imaging, and other fields requiring high-precision measurements on non-planar surfaces, where conventional techniques often compromise accuracy, speed, or system complexity.

This paper is organized into the following sections. Section 2 details the principles and methods of the proposed three-dimensional measurement of fiber end face position. Section 3 presents the experimental measurement system. Section 4 discusses the results of the method. Section 5 provides the conclusion.

2. Method

The 3D measurement method proposed in this paper enables precise 3D measurement of the LAMOST fiber end-face by processing images of the focal plane fibers captured from different angles. The methodology includes three key parts: (1) extraction of spot center based on grayscale distribution model; (2) the decoding method of coding points based on clustering and pattern matching; and (3) 3D reconstruction method based on SFM and coded information. The overall solution flowchart is shown in figure 1.

An overview diagram of our setup is provided in detail in figure 2. In our setup, the camera and the front-illumination source are positioned 2 meters in front of the fiber end face and 3.5 meters to the right of the focal plane, respectively, while a device integrating the spectrometer and a back-illumination source is placed behind the focal plane.

The LAMOST simulation system contains a total of 15 optical fibers. During normal operation, the measured light passes from the front of the focal plane through optical fibers into the spectrometer, while during fiber end-face position measurements, the end-face of the optical fiber will be illuminated by a back-illumination source for the determination of its position. The imaging strategy entails capturing sequential frame images through the motion of a single camera, while integrating both front and back lighting sources. Specifically, at each shooting location, two images are captured: a front-illuminated image, taken with the front light turned on, to extract coding points information; and a back-illuminated image, taken with only the back-illumination source active, to extract fiber spot data.

2.1. Extraction of spot center based on grayscale distribution model

Accurate extraction of key feature points, specifically the 2D spot centers of photographed fibers and coded points, is crucial for 3D measurement of the LAMOST focal plane fiber end-face. The 2D coordinates of these key feature points are essential for multiple stages of the 3D measurement process. We developed the extraction of spot center based on ES-GDM. The model comprises three steps: spot identification under multiple constraints, bilateral filtering with adaptive weights, and spot center extraction using adaptive threshold segmentation.

When acquiring LAMOST focal plane spot images, interference from noise and deformation is inevitable (Yang *et al* 2024), as shown in figure 3. Traditional methods such as threshold segmentation, template matching, and machine learning struggle to achieve optimal spot recognition. Therefore, we propose a multi-constraint recognition method based on the differences in gray-scale distribution between light spots, background, and clutter. We observe that light spots exhibit the following characteristics compared to background and interference clutter: (1) higher average gray value, (2) nearly elliptical shape, and (3) consistent size. These features enable accurate spot identification, so we define three constraint criteria: mean gray value, contour, and size, to ensure precise spot recognition in the focal plane image.

However, the presence of noise in the spot region can hinder accurate spot center extraction. To reduce noise and enhance spot center extraction accuracy, we evaluated various filtering algorithms, selected the bilateral filter (Gavaskar and Chaudhury 2018), and further improved its performance. This methodology preserves edge information while effectively filtering noise, as shown below:

$$\hat{I}(x,y) = \frac{\sum\limits_{(i,j)\in S_{x,y}} W(x,y) \times I(i,j)}{\sum\limits_{(i,j)\in S_{x,y}} W(i,j)} \tag{1}$$

where $I(x,y)$ represents the noise-containing image, $\hat{I}(x,y)$ is the filtered image, $S_{x,y}$ is the set of spatial neighborhoods within the filter window, and $W(x,y)$ is the total bilateral filter weight.

Given that the gray values of the spot image follow an approximate normal distribution, we use the global gray standard deviation as the standard deviation for pixel values in the bilateral filtering. The filter window size is set to 3 to match the spot size.

Analysis of the acquired LAMOST fiber and coding point spot images revealed that the gray value distributions of both approximately follow a Gaussian distribution (Sun and Xie 2023), as shown in figure 4.

We also generated the grayscale histograms for the encoding point and fiber spot, as shown in figure 5. These histograms exhibit two prominent Gaussian distribution features, where the lower and higher grayscale regions correspond to the background and spot grayscale characteristics, respectively.

Using the Gaussian-distributed spot shape from figure 4 and the grayscale histogram features from figure 5, we set the grayscale value at the standard deviation of the first approximate Gaussian distribution as the adaptive segmentation threshold I_{tr}, as shown in equation (2). This dynamic threshold setting not only preserves the spot's edges but also reduces the extraction error of the grayscale center of gravity method,

$$I(i,j) = \begin{cases} I(i,j), (I(i,j) \geqslant I_{\mathrm{tr}}) \\ 255, (I(i,j) < I_{\mathrm{tr}}) \end{cases} \tag{2}$$

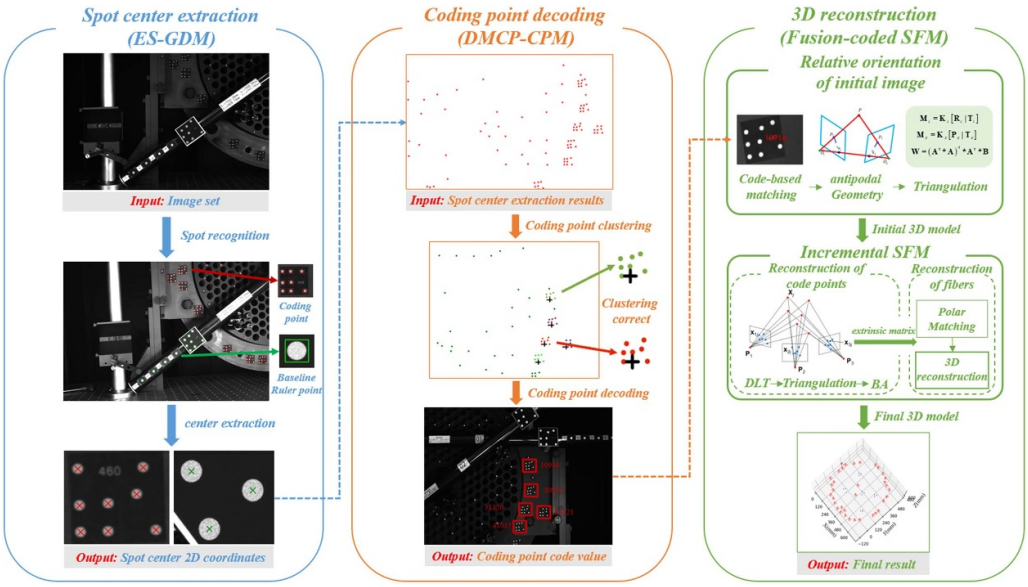

Figure 1. Overall solution flowchart.

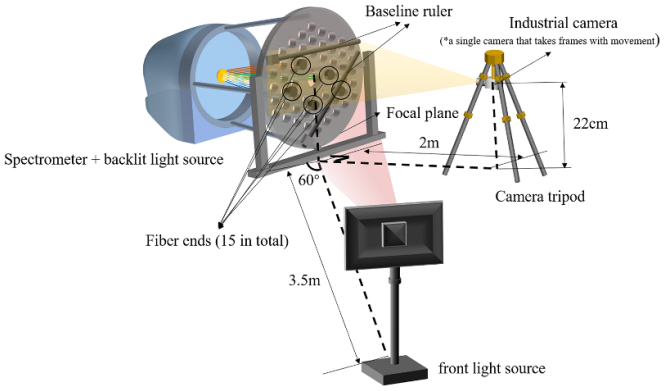

Figure 2. Overview diagram of the setup.

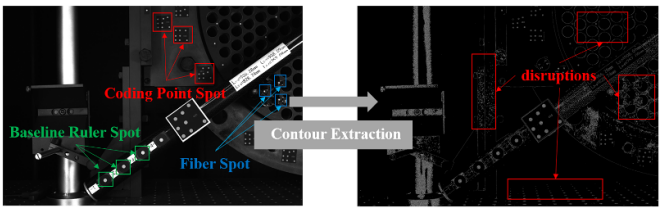

Figure 3. Edge skeleton line extraction result.

where $I(i,j)$ represents the gray value at (i,j).

The exact location of the spot center can be determined by the gray center of gravity method, which calculates the weighted average of the gray values and coordinates of all pixel points in the segmented image, as expressed below:

$$x_0 = \frac{\sum_{x=0}^{M-1}\sum_{y=0}^{N-1} xf(x,y)}{\sum_{x=0}^{M-1}\sum_{y=0}^{N-1} f(x,y)}, y_0 = \frac{\sum_{x=0}^{M-1}\sum_{y=0}^{N-1} yf(x,y)}{\sum_{x=0}^{M-1}\sum_{y=0}^{N-1} f(x,y)} \quad (3)$$

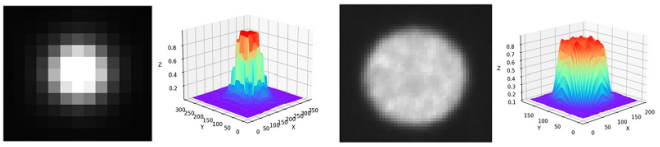

Figure 4. Fiber (right) and coding point (left) spots and their grayscale distribution.

where $f(x,y)$ is the gray value of the pixel point, M,N are the length and width of the image, and x_0,y_0 are the center coordinates of the target spot.

2.2. The decoding method of coding points based on clustering and pattern matching

After extracting the center of the key feature spot, the next crucial step in solving the extrinsic matrix of the camera at different positions using the structure from motion (SFM) (Schonberger and Frahm 2016) method is to match the key feature points across each frame. However, fiber images taken under back illumination lack distinct texture features, rendering traditional SFM feature matching methods (e.g. SIFT Lowe 1999, SURF Bay *et al* 2008), which rely on corner and edge points, unsuitable for this task. To address this, we match key feature points across frames using coding points, which are clearly imaged and contain encoded information. To address this, we assist in matching key feature points across different frames by using coded points, which are more clearly imaged and contain coded information.

In this paper, we utilize point coding, with the design principle illustrated in figure 6. The system includes 33 points: 5 template points and 28 decoding points. Each group of coding points contains 8 points: 5 template points and 3 decoding points selected from the 28 available. In figure 6, points A, B,

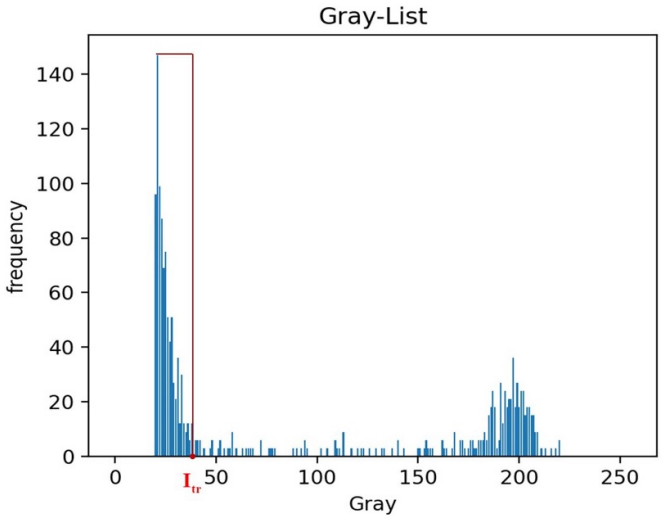

Figure 5. Histogram of grayscale of spot image.

C, D, and E are template points. Point C is the coordinate origin, with $\overline{CD}$ and $\overline{CB}$ representing the x and y axis directions, respectively, and points A, C, and E lying on the same line.

Based on the design principle of coding points, we developed a decoding method of coding points based on clustering and pattern matching (DMCP-CPM), consisting of two steps: coding point identification using an improved clustering algorithm and coding point decoding through pattern matching.

First, we identify the coding point clusters by clustering the light spots. Light spots belonging to the same coding point group are categorized into a single cluster, and the number of clusters corresponds to the number of coding point groups in the image. The scatter distribution analysis is shown as figure 7. Classical clustering algorithms, such as division-based K-Means (MacQueen *et al* 1967) and density-based DBSCAN (Ester *et al* 1996), struggle to accurately cluster coding point groups. K-Means is sensitive to noise and outliers because it relies on the initial cluster centers, while DBSCAN heavily depends on neighboring parameter settings, making it difficult to separate clusters with close densities but distant locations. Therefore, inspired by the K-distance concept, we propose an improved clustering algorithm.

The method consists of four main steps: (1) Find the distance set based on K-distance: traverse the initial point set $C_{\mathrm{p}} = \{p_1, p_2, \cdots, p_m\}, p_m = (x_i, y_i)$, calculate the distance between each point and the remaining points, and generate the corresponding distance set and point set. (2) Obtain the bounding box: calculate the bounding box of the points in the set and continuously update B based on $B = B \cup \{x_{im}, y_{im}\}$; (3) Apply thresholding based on second-order difference: since the data in the distance and bounding box sets are discrete, and contain inflection points, these inflection points in the distance set are used as thresholds based on second-order differences; (4) Clustering: finally, use the threshold to filter and eliminate duplicate items, achieving clustering.

After identifying the coded points through clustering, we apply the pattern matching principle for decoding. This

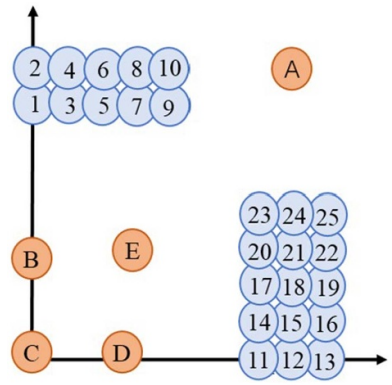

Figure 6. Schematic diagram of coding point design.

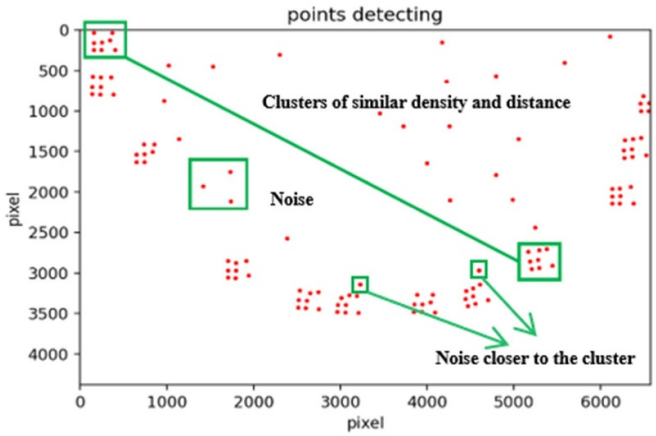

Figure 7. Scatter distribution analysis.

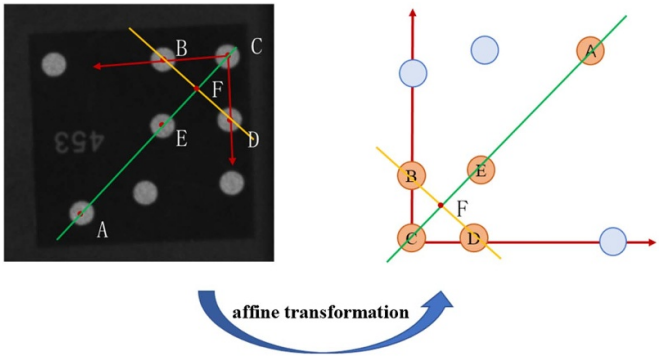

Figure 8. Affine transformation schematic.

involves matching the actual image point set with the template point set to achieve the mapping from the actual coordinate system of the coded points to the designed coordinate system, as shown in figure 8.

In figure 8, if the intersection of points B and D is denoted as F, then the points C, F, E, and A are collinear. The matching of these four points with the template points in the design coordinate system can be achieved using the invariance of their intersection ratio, as shown in equation (4). Next, the affine transformation matrix is calculated using the least squares method (see equation (5)), mapping the coordinates

of the decoding points from the actual coordinate system to the design coordinate system to determine the coding point number,

$$R_{L(A,E,F,C)} = \frac{\overline{AF}\cdot\overline{EC}}{\overline{EF}\cdot\overline{AC}}, \tag{4}$$

$$\begin{bmatrix} x' \\ y' \end{bmatrix} = \begin{bmatrix} a & b \\ d & e \end{bmatrix} \begin{bmatrix} x \\ y \end{bmatrix} + \begin{bmatrix} c \\ f \end{bmatrix} \tag{5}$$

where a,b,c,d denote the rotation, distortion and scaling between the design coordinate system and the actual coordinate system, c,f denote the translation between the two coordinate systems. x,y represent the coordinates in the actual coordinate system, and x',y' represent the coordinates in the design coordinate system.

2.3. 3D reconstruction method based on SFM and coding information

By utilizing the matching information of the corresponding coding points in the images from different frames, we developed a 3D reconstruction method based on incremental SFM and coding information (Fusion-coded SFM).

2.3.1. Relative orientation of the initial two image frames.

Determining the relative orientation of the initial two image frames is essential for constructing a high-precision 3D model (Zhou *et al* 2024). We first use the center coordinates of matched coding points to estimate the fundamental matrix between the images, then calculate the relative position and orientation between them. Let point P be a point in 3D space, with coordinates $P=[X,Y,Z,1]^{\mathrm{T}}$ in the coordinate system of the first frame (the world coordinate system). Points P_1 and P_2 represent the image points of P on the two image frames, and their relationship is constrained by epipolar geometry, as shown below:

$$P_2^{\mathrm{T}}\left(K^{-1}\right)^{\mathrm{T}} EK^{-1}P_1 = 0 \tag{6}$$

where K represents the camera intrinsic parameters and E denotes the essential matrix.

For a single image point, the fundamental matrix equation can be expressed as in equation (7), solving the matrix using the eight-point method with corresponding coded points. Equation (7) expresses the epipolar constraint for a pair of corresponding points (x_1,y_1) and (x_2,y_2) in two images, where the vector contains combinations of their coordinates used to form a linear equation for estimating the fundamental matrix F,

$$\begin{bmatrix} x_1x_2 & x_1y_2 & x_1 & y_1x_2 & y_1y_2 & y_1 & x_2 & y_2 & 1 \end{bmatrix} F = 0. \tag{7}$$

Next, using the relationship between the fundamental matrix and the intrinsic matrix K as $F=\left(K^{-1}\right)^{\mathrm{T}}EK^{-1}$, the essential matrix E can be solved. The essential matrix E is a singular matrix of rank 2 with two identical nonzero singular values, denoted as σ. Let the singular value decomposition (SVD) of E be represented as below:

$$E = U\Sigma V^{\mathrm{T}} \tag{8}$$

where U and V are orthogonal matrices, and Σ is the singular value matrix. For any E, there are two possible corresponding t,R matrices, as follows:

$$\begin{cases} [t_1]_\times = UR_z\left(\frac{\pi}{2}\right)\Sigma U^{\mathrm{T}}, R_1 = UR_z^{\mathrm{T}}\left(\frac{\pi}{2}\right)V^{\mathrm{T}} \\ [t_2]_\times = UR_z\left(-\frac{\pi}{2}\right)\Sigma U^{\mathrm{T}}, R_2 = UR_z^{\mathrm{T}}\left(-\frac{\pi}{2}\right)V^{\mathrm{T}} \end{cases} \tag{9}$$

where $R_Z\left(\frac{\pi}{2}\right)$ represents the rotation matrix obtained by rotating 90 degrees around the specified axis.

Since $-E$ and E are equivalent, applying a negative sign to any t yields the same result. Consequently, after SVD decomposition, four sets of solutions for R and t are obtained. Of the four possible solutions, only the one where the object point is located in front of the camera in both frames (i.e. both camera depths are positive) is retained. This is verified using the cheirality condition as discussed in Hartley (2003). To determine the correct physical solution among the four, we evaluate each by triangulating a set of corresponding feature points from the two views and checking the cheirality condition, which asserts that the reconstructed 3D point must lie in front of both cameras. Mathematically, this means the depth values of the triangulated points must be positive when projected onto the coordinate system of both camera frames. Therefore, the only valid solution is the one in which the majority (or all) of the reconstructed points satisfy this positive depth criterion in both camera frames. Finally, the initial values of the rotation matrix R and translation matrix t between the first two frames are obtained.

After obtaining the extrinsic matrix of the two image frames, triangulation is used to estimate the spatial positions of the image points. Let $\mathbf{M}_L=\mathbf{K}_L[\mathbf{R}_L \mid \mathbf{T}_L]$ and $\mathbf{M}_p=\mathbf{K}_p[\mathbf{P}_p \mid \mathbf{T}_p]$ represent the projection matrices of the camera at two different positions, and (u_L,v_L) and (u_R,v_R) denote the corresponding 2D coordinates of the 3D point P in the two image frames. The 3D coordinates of the point are then computed using the least squares method, as shown below:

$$\boldsymbol{P} = \left(\boldsymbol{A}_{\mathrm{LSM}}{}^{\mathrm{T}}\cdot\boldsymbol{A}_{\mathrm{LSM}}\right)^{-1}\cdot\boldsymbol{A}_{\mathrm{LSM}}{}^{\mathrm{T}}\cdot\boldsymbol{B}_{\mathrm{LSM}} \tag{10}$$

where:

$$\boldsymbol{A}_{\mathrm{LSM}} = \begin{bmatrix} M_{L0,0}-M_{L2,0}u_L & M_{L0,1}-M_{L2,1}u_L & M_{L0,2}-M_{L2,2}u_L \\ M_{L1,0}-M_{L2,0}v_L & M_{L1,1}-M_{L2,1}v_L & M_{L1,2}-M_{L2,2}v_L \\ M_{R0,0}-M_{R2,0}u_R & M_{R0,1}-M_{R2,1}u_R & M_{R0,2}-M_{R2,2}u_R \\ M_{R1,0}-M_{R2,0}v_R & M_{R1,1}-M_{R2,1}v_R & M_{R1,2}-M_{R2,2}v_R \end{bmatrix} \tag{11}$$

$$\boldsymbol{B}_{\mathrm{LSM}} = \begin{bmatrix} u_LM_{L2,3}-M_{L0,3} \\ v_LM_{L2,3}-M_{L1,3} \\ u_RM_{R2,3}-M_{R0,3} \\ v_RM_{R2,3}-M_{R1,3} \end{bmatrix}. \tag{12}$$

2.3.2. Coding and fiber point reconstruction based on incremental SFM. After completing the relative orientation of the initial two-frame images, the generated 3D model serves as the initial value (Zheng *et al* 2013). First, coding information and incremental SFM are utilized to achieve the 3D reconstruction of the coding points and to determine the camera extrinsic parameter matrix. Subsequently, the intrinsic and extrinsic parameter matrices are employed as a prior conditions to reconstruct the fiber points in 3D.

After adding each new frame, we assess whether there are common points with the reconstructed coded points. When a new frame is introduced, we identify clusters with the same encoded value as those in previously reconstructed frames. If a cluster with matching code is found in both frames, then all 8 points in the cluster can be deterministically matched with 100% precision, due to the rigid spatial configuration formed by five template points and the unique identification enabled by three decoding points in each 8-point coded cluster as shown in figure 6. This leads to a highly efficient and reliable matching process, achieving an average matching time of 0.0203 s for five coded clusters (40 points) across two frames, without the need for complex computations or optimization-based matching strategies. If common points are identified, the 2D–3D matching is performed on the basis of the coding information. Then the direct linear transformation (DLT) (Shapiro 1978) method is used for bitmap estimation in the newly added frame images. Unlike the traditional 2D–2D method, DLT is a 3D–2D approach that ensures consistent bit-position estimation across different scales. If the image coordinate of a given image point is $[x, y, 1]^{\mathrm{T}}$ and its corresponding 3D point coordinate is $[X, Y, Z, 1]^{\mathrm{T}}$, a linear relationship between the two can be established using the coefficient matrix L as follows:

$$\begin{bmatrix} x \\ y \\ 1 \end{bmatrix} = \boldsymbol{L} \begin{bmatrix} X \\ Y \\ Z \\ 1 \end{bmatrix}. \tag{13}$$

After obtaining the set of camera extrinsic matrices, triangulation is applied to reconstruct the 3D coordinates of coding points that are common to the current and previous frames but have not yet been reconstructed. However, a reprojection error e exists between the projected 3D points on the image plane and the actual measured image points. By minimizing this error, the 3D coordinates and extrinsic matrix can be further optimized.

Let P_j represent the 3D coordinates of a specific coding point. The coordinates of the corresponding image point in the first image can be calculated as p_{ij} based on the camera parameters, as shown below:

$$p_{ij} = K[R \mid t] P_j \tag{14}$$

where K is the intrinsic matrix, R and t are the rotation matrix and translation vector representing the extrinsic parameters of the camera.

To minimize the reprojection error, the maximum likelihood estimate of the transformation matrix between the 3D coordinates of the coding points and the images from each frame is derived according to follows:

$$\min \sum_i \sum_j \left(\tilde{\boldsymbol{p}}_{ij} - \boldsymbol{K}[\boldsymbol{R}_i \mid \boldsymbol{t}_i] \boldsymbol{P}_{\mathrm{j}}\right)^2 \tag{15}$$

where $\tilde{p}_{ij}$ represents the coordinates of the image point corresponding to P_j in the first image, extracted using the ES-GDM method. In this equation, R_i and t_i are the rotation matrix and translation vector representing the extrinsic parameters of the camera for the ith image, respectively.

The trust region reflective (Le *et al* 2017) method is employed to solve the nonlinear least squares problem in beam method leveling. This method updates parameters by calculating the first-order derivatives (Jacobian matrix) and second-order derivatives (Hessian matrix) of the objective function. The trust region constrains parameter updates, ensuring variation within a specific range.

After completing the 3D reconstruction of all coding points, utilizing the optimized set of camera extrinsic matrices, the 3D reconstruction steps for fiber optic points are outlined as follows:

(1) Retrieve the camera extrinsic matrix $\left(H_{\mathrm{ml}}, H_{\mathrm{mr}}\right)$ from the set of extrinsic matrices $\{H\}$ for the two frames of image $\left(I_{\mathrm{m1}}, I_{\mathrm{mr}}\right)$ that share a common fiber point, and then solve for the fundamental matrix F.

(2) Calculate the epipolar line L_i in right image I_{mr} (Assume that the equation of the polar line L_i satisfies $a_i x + b_i y + c_i = 0$) corresponding to the point $\boldsymbol{p}_{li} = (x_{li}, y_{li})$ in left image I_{m1} using

$$l_i = F p_{li}. \tag{16}$$

According to the principles of epipolar geometry, a 3D point observed from a point of view $\boldsymbol{p}_{li} = (x_{li}, y_{li})$ in the left image I_{m1} will project onto the epipolar line L_i ($a_i x + b_i y + c_i = 0$) in the right image I_{mr}. In the ideal case, the perpendicular distance from point $\boldsymbol{p}_{ri} = (x_{ri}, y_{ri})$ in I_{m1} corresponds to the matching point of $\boldsymbol{p}_{li} = (x_{li}, y_{li})$ to the epipolar line L_i should be 0. Therefore, the epipolar constraint is utilized to filter the set of points in the right image.

(3) Calculate the perpendicular distance d_i from each point $\boldsymbol{p}_{rj} = (x_{rj}, y_{rj})$ in I_{mr} to the polar line L_i (satisfies $a_i x + b_i y + c_i = 0$), and add the points that satisfy equation (17) to the set of candidate image points with the same designation,

$$d_i = \frac{|a_i x_{rj} + b_i y_{rj} + c_i|}{\sqrt{a_i^2 + b_i^2}} < d_{\mathrm{t}} \tag{17}$$

where d_t represents the maximum distance threshold that must be satisfied at that point. It is usually set to 5 pixels.

(4) Sort the distance sets in the candidate same-name image point set, retain the point with the smallest distance as the corresponding matching point of $\boldsymbol{p}_{li} = (x_{lj}, y_{lj})$, and complete the screening in the point set to eliminate the 'false image points' and obtain the fiber optic point matching information.

Repeated experiments conducted on five image pairs showed that the minimum distances from all points (Points $\boldsymbol{p}_{rj}$) to their corresponding epipolar lines are consistently less than 0.5 pixels. Moreover, the ratio between the second smallest distance (within the threshold range) and the smallest distance exceeds a factor of 10. This significant difference in epipolar distances clearly distinguishes correctly matched points from false correspondences, achieving 100% filtering accuracy with an average processing time of 0.0052 s per image pair. Such a distinction ensures the effective elimination of 'false image points'.

(5) The 3D coordinates of the fiber points are reconstructed based on the coding point 3D reconstruction process.

2.3.3. Model scale adjustment. After obtaining the fiber point data through incremental reconstruction, the baseline ruler is reconstructed simultaneously to calculate the scaling factor. This ensures that the reconstructed point model closely matches the real object (Bernardini *et al* 2016). The global model is then scaled according to the calculated scaling factor. Since s is applied as a multiplicative factor to scale the entire 3D point cloud from the reconstruction space to the real-world metric space, the deviation of s will propagate linearly into absolute distance measurements. The deviation in the scale factor s is primarily attributed to the metrological error of the two baseline ruler lengths $\bar{D}_{\mathrm{a}}$ and $\bar{D}_{\mathrm{b}}$ characterized by calibration. In our study, the reference lengths were calibrated and certified by a national metrology institute, with traceable verification reports provided. Consequently, the calibration uncertainty of these reference standards is exceptionally low (<0.001 mm), thereby minimizing potential bias in the derived scale factor to the greatest extent possible. First, the 2D coordinates of the endpoints of the baseline ruler and the extrinsic matrix of the corresponding frame are extracted. Let e_0 and e_1 represent the two endpoints of the baseline used in our experimental setup. The three-dimensional coordinates of these two points are given by $(X_{\mathrm{e}0}, Y_{\mathrm{e}0}, Z_{\mathrm{e}0})$ and $(X_{\mathrm{e}1}, Y_{\mathrm{e}1}, Z_{\mathrm{e}1})$, respectively. The baseline ruler is then reconstructed using the same method as for the fiber optic points, and its length d is calculated as follows:

$$d = \sqrt{(X_{\mathrm{e}1} - X_{\mathrm{e}0})^2 + (Y_{\mathrm{e}1} - Y_{\mathrm{e}0})^2 + (Z_{\mathrm{e}1} - Z_{\mathrm{e}0})^2}. \quad (18)$$

Assuming the calibrated lengths of the two datum rulers are $\bar{D}_{\mathrm{a}}$ and $\bar{D}_{\mathrm{b}}$, and the lengths obtained from the 3D reconstruction of the point cloud are D_a and D_b. The formula for the global scale factor s is obtained by combining the individual scale factors of the two calibration scales ($s_a = \frac{\bar{D}_a}{D_a}$ and $s_b = \frac{\bar{D}_b}{D_b}$) using a weighted average method, where the weights of the weighted average are the squares of the calibration lengths of the two baseline rulers ($w_a = \bar{D}_a^2$ and $w_b = \bar{D}_b^2$). The global model scale factor s is calculated as shown below:

$$s = \frac{w_a s_a + w_b s_b}{w_a + w_b} = \frac{D_b \bar{D}_a^3 + D_a \bar{D}_b^3}{D_a D_b \left(\bar{D}_a^2 + \bar{D}_b^2\right)}. \quad (19)$$

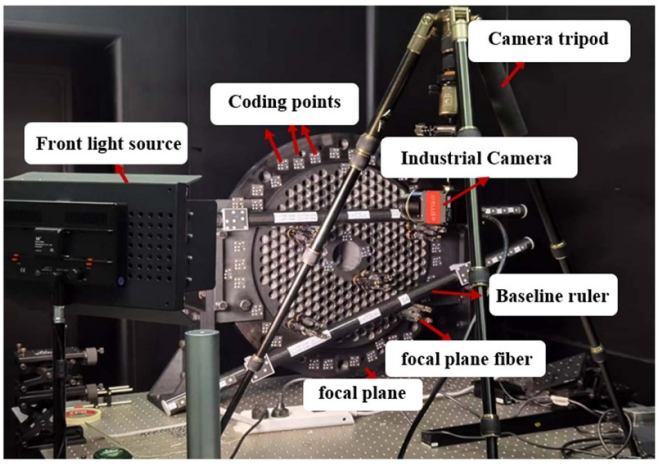

Figure 9. Constructed experimental setup system.

To account for the imaging difference between the two perpendicular directions of the image, we incorporated two baseline rulers in the scene. These two rulers were deliberately placed in approximately orthogonal directions, one nearly horizontal and the other with a relatively large inclination as shown in figure 9. This setup ensures that horizontal and vertical rulers could be given, thereby mitigating the directional bias in the scale estimation.

3. Integral measuring systems

To achieve the 3D measurement of the LAMOST focal plane fiber end-face position, we designed a monocular vision-based measurement system and constructed a test platform at the National Astronomical Observatories of China. This section details the hardware components of the system and the measurement workflow for the acquired images.

3.1. Measurement system construction

The experimental platform of the measurement system is shown in figure 9. The main hardware includes: (1) Industrial camera: AVT GT6600 industrial camera, with a high-resolution 35 mm CCD sensor, offering approximately 30 million effective pixels; (2) Lens: Schneider EMERALD 2.2/50 F lens, with a 50 mm fixed focal length and an aperture range of F2.2–F16; (3) Baseline ruler and coding points: the baseline ruler is a carbon fiber rod used as a scale reference; (4) Light source: LS LED 508A, operating at 7.4 V–14.8 V DC and 30.5 W, providing adjustable white light illumination for the coding points.

Due to the small size of the fiber in the image, it can easily be overwhelmed by coding and stray spots, making extraction difficult. Therefore, when capturing the fiber spot, we turn off other light sources and activate the spectrometer to illuminate the fiber using a back illumination method. For the coding spots, we use the front-illuminated adjustable light source to capture the spot image. The acquired images of the fiber and coding spots are shown in figures 10 and 11, respectively.

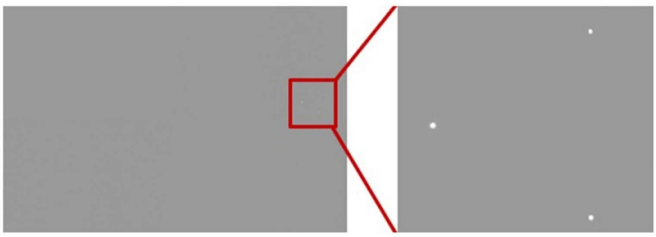

Figure 10. Back illumination image.

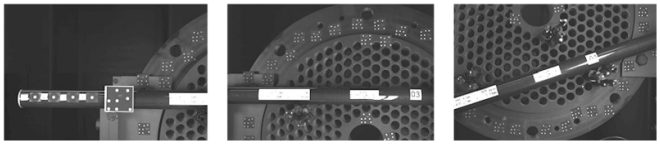

Figure 11. Front illumination image.

3.2. Design of the measurement process

The block diagram of the measurement process is presented in figure 12, with the following steps:

(1) First, two front-illuminated images containing coding points are selected. The centers of all spots are extracted, and the coding points are decoded. The fundamental matrix between the two images is then calculated using the corresponding coding points, followed by polar matching of non-coded points.
(2) Align the matched points in the two images and solve for the camera position to obtain the extrinsic matrix. Using the camera's intrinsic and extrinsic matrix, apply the least squares method to reconstruct all matched points in 3D, resulting in the optimized camera extrinsic matrix and the 3D coordinates of the matched points.
(3) Select two fiber-optic images taken using back-illumination at the same viewing angle as in step (1). Extract the centers of the fiber spots, match them, and perform 3D reconstruction using the fundamental matrix and camera extrinsic matrix obtained in step (2), ultimately acquiring their 3D coordinates.
(4) Gradually incorporate images from new viewpoints and use incremental SFM to accurately determine the 3D coordinates of all fiber end faces, transforming them into a common coordinate system. Follow the same steps to reconstruct the baseline scale and calculate its base length and scale factor s. Finally, apply the scale factor s to assign the true physical scale to the entire 3D model and evaluate the reconstruction results.

4. Result

4.1. Spot identification and center extraction

First, we performed a spot recognition experiment on the acquired LAMOST focal plane image set, using the multiple-constraints-based method proposed in section 2.1. The visualization of the experimental results is presented in figure 13.

The dataset consists of 1474 light spots. Among these, 1251 coding point light spots were identified, yielding an identification rate of 98.0%. For 106 baseline ruler light spots, 104 were identified, resulting in an identification rate of 98.1%. All 117 fiber light spots were successfully identified, achieving an identification rate of 100%. Thus, the different light spots were successfully classified. The experimental results are summarized in table 1.

To quantitatively analyze the quality of the filtered images, we conducted experiments using a mean filter, Gaussian filter, bilateral filter, and the adaptive weighted bilateral filter proposed in this paper. These experiments were performed on simulated spots, fiber spots, and coding point spots, with the results presented in table 2. The results indicate that the adaptive weighted bilateral filter outperforms the others in terms of PSNR, ENL, EPI, and SSIM, demonstrating the method's superiority. This finding confirms that adaptive weighted bilateral filtering effectively removes noise while preserving the edges of spot images. These advantages make it particularly suitable for denoising spot images on the LAMOST focal plane.

Finally, we conducted experiments to extract the centers of the light spots. However, because the true position of the spot center in the captured image is unknown, we first simulated and generated a Gaussian spot containing noise, as illustrated in figure 14. Next, we simulated 20 light spots with varying sizes and gray values that conform to a Gaussian-like distribution, generated on an image matching the camera's pixel dimensions (6576 $\times$ 4384 pixels). Subsequently, we introduced Gaussian noise with varying standard deviations and conducted four comparison experiments. To compare the effectiveness of different spot center extraction algorithms, we used the center coordinate deviation rate as the accuracy evaluation metric, as $\eta = \frac{d_0}{r} \times 100\%$. Here, d_0 denotes the distance between the extracted spot center and the actual spot center, while r represents the radius of the actual spot.

We employed several methods for spot center extraction and comparison: the ellipse fitting method, the Hessian matrix method, the fixed threshold grayscale center of gravity method, the grayscale center of gravity method with Otsu threshold segmentation, and the extraction of ES-GDM, proposed in this paper. Figure 15 presents the experimental results for the center coordinate deviation rate.

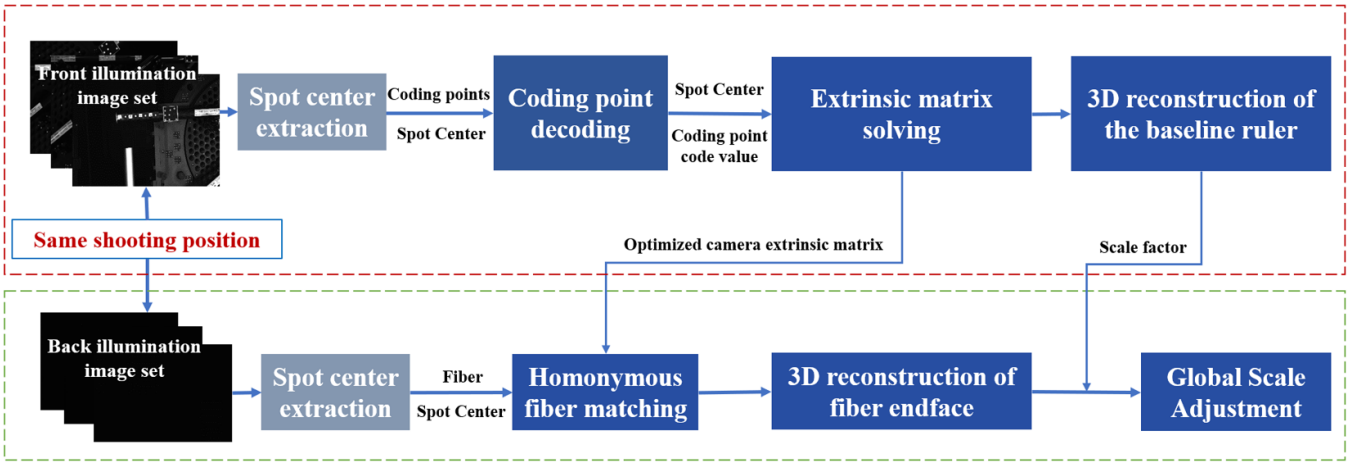

Figure 12. Flow chart of fiber end-face position measurement.

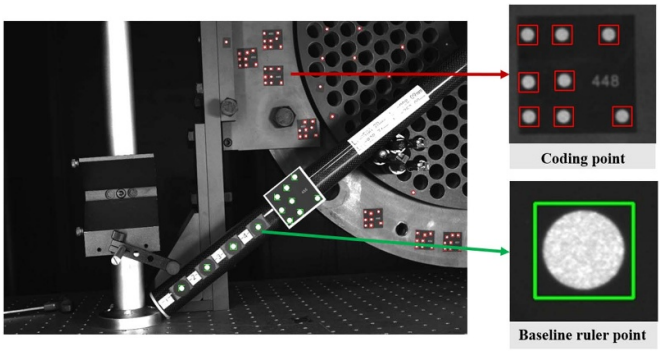

Figure 13. Spot recognition results.

Table 1. Experimental results of spot recognition.

Spot type	Actual number	Number of identified	Missed detection	False detection	Recognition rate
Coding point spot	1251	1244	16	9	98.0%
Baseline ruler spot	106	104	2	0	98.1%
Fiber optic spot	117	117	0	0	100%
Total spot	1474	1465	18	9	98.7%

Table 2. Filtering comparison experimental results.

Spot type	Filtering method	PSNR	ENL	EPI	SSIM
Simulated spot	Mean value	35.7413	1.1222	0.7708	0.9069
	Gaussian	35.9036	1.1321	0.6919	0.9238
	Bilateral	37.1838	1.1230	0.8197	0.9319
	Ours	37.2951	1.1228	0.8461	0.9356
Fiber spot	Mean value	42.0522	0.3100	0.7670	0.9962
	Gaussian	37.5368	0.3125	0.6472	0.9824
	Bilateral	54.1501	0.3102	0.8748	0.9882
	Ours	55.6758	0.3102	0.9283	0.9986
Coding point spot	Mean value	39.0632	2.1243	0.5771	0.9778
	Gaussian	36.9879	2.1367	0.3683	0.9628
	Bilateral	44.2988	2.1275	0.6789	0.9885
	Ours	47.6093	2.1251	0.8211	0.9935

The red bold line in figure 15 illustrates the variation curve of the center coordinate deviation rate for the ES-GDM method proposed in this paper. The results indicate that the spot center coordinate deviation rate increases with rising noise levels. The ellipse fitting method and the fixed threshold grayscale center of gravity method exhibit less stability, whereas the Hessian matrix-based method demonstrates the smoothest variation curve and the highest stability, followed closely by the ES-GDM method.

Table 3 presents the average absolute errors and time consumption comparisons of the different algorithms applied to images with Gaussian noise added at varying standard deviations (1, 1.5, 2, 2.5).

Table 3 indicates that the Hessian matrix-based method achieves the highest extraction accuracy, followed by the ES-GDM method, which is significantly more accurate than both the fixed threshold grayscale center of gravity method and the grayscale center of gravity method with Otsu threshold segmentation. The ES-GDM method has the shortest detection time of 1.085 s, while the Hessian matrix-based method requires the longest time of 11.074 s, which is 10.206 times longer than that of the ES-GDM method.

Based on the experimental results presented above, the ES-GDM method proposed in this paper effectively enables the extraction of the spot center on the LAMOST focal plane with both high efficiency and high precision.

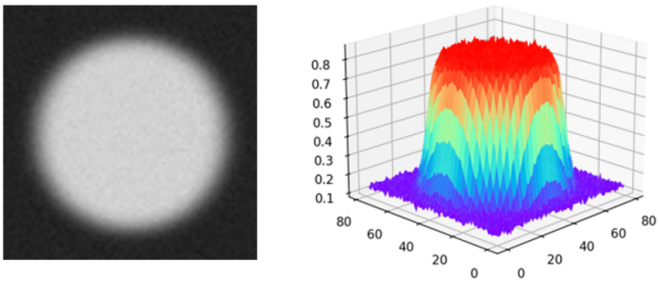

Figure 14. Schematic diagram of the simulated light spot.

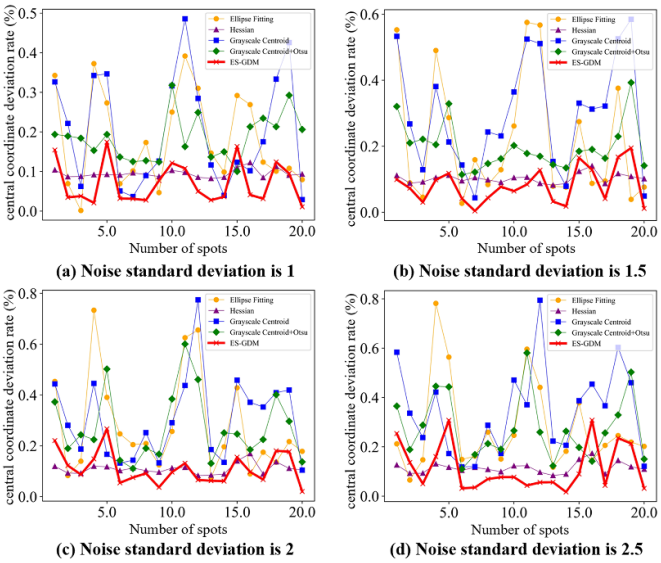

Figure 15. Experimental results of deviation rate of center coordinates.

Table 3. Spot center extraction algorithm consumption time comparison.

Method	Mean absolute error (pixel)	Time (s)
Ellipsoid fitting method	(0.059,0.045)	1.046
Hessian matrix method	(0.005,0.005)	11.074
Gray scale center of gravity method	(0.062,0.058)	1.085
OTSU-based gray scale center of gravity method	(0.027,0.035)	1.392
ES-GDM(ours)	(0.018,0.012)	1.085

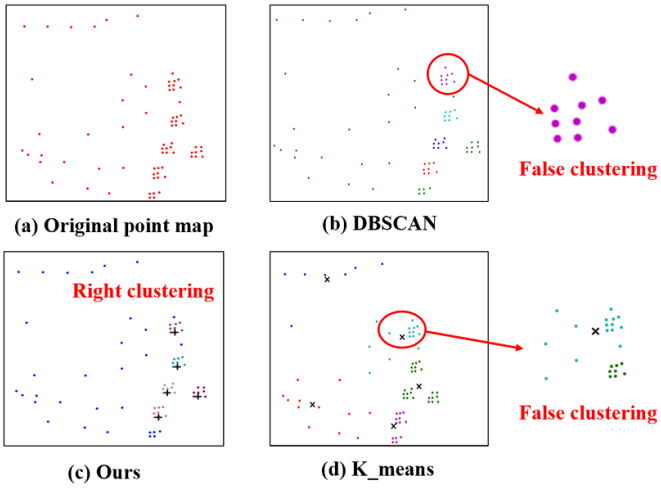

Figure 16. Comparison of clustering effects.

4.2. Coding point clustering and decoding

After extracting the coordinates of the spot centers, we conducted experiments on coded spot clustering and decoding. Figure 16 presents a comparative plot of the clustering effects of the light spots in the LAMOST focal plane image. In the figure, different colors represent distinct clustering categories, corresponding to different clusters of coded spots, while the symbol $\times$ denotes the clustering center. In our experiments, the parameter *Minpts* is set to 8, the neighborhood parameter ε for DBSCAN is determined by the screening threshold q calculated by our algorithm, and the number of clusters for K-Means is set to 5.

In our design (as illustrated in figure 16), a correct coding cluster is expected to comprise eight points arranged according to a specific geometric configuration. Figure 16 demonstrates that, for the DBSCAN method, the purple cluster not only encompasses the actual coding points but also erroneously includes neighboring noise points, leading to the misclassification of unrelated data. Similarly, issues arise with the k-means method: the blue cluster incorporates nearby noise points, and more critically, the green cluster incorrectly merges two distinct real clusters into one, thereby violating the design principles. The findings indicate that neither the K-Means nor the DBSCAN method achieves accurate clustering of coding points, whereas the method proposed in this paper successfully accomplishes precise clustering of coding points.

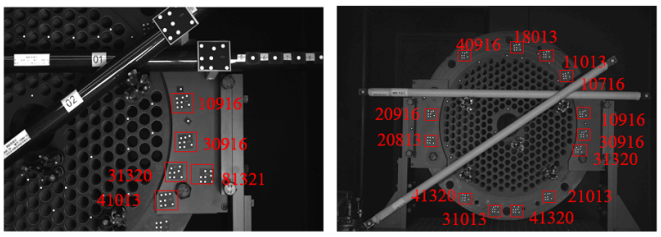

Figure 17. Visualisation of decoding results.

To further validate the effectiveness of the decoding algorithm presented in this paper, we conducted decoding experiments on the coded points in the focal plane image across different fields of view. Figure 17 illustrates the decoding visualization results for different fields of view, where (a) represents a small field of view and (b) represents a large field of view. The experimental results demonstrate that the method proposed in this paper achieves fully automatic decoding of all coded points across varying fields of view.

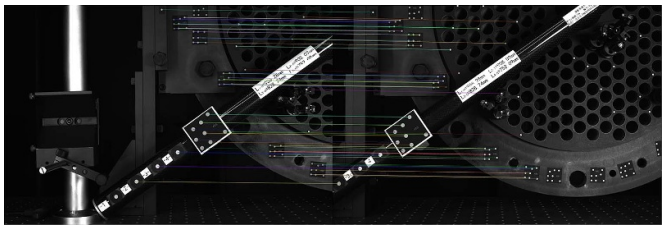

Figure 18. Coding point matching Results.

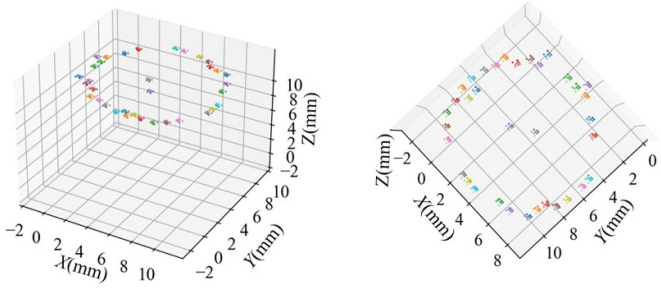

Figure 19. Coding point 3D reconstruction results.

4.3. Coding point matching and 3D reconstruction

First, we use the decoding information to complete the matching of all the common coding points in the image, in which the matching results of the common coding points in the two images are shown in figure 18 for example.

Subsequently, using the images from the front-illuminated image set, we perform 3D reconstruction of all coding points on the focal plane to obtain the extrinsic matrix for each frame, along with the 3D coordinates of all coding points. The 3D reconstruction visualizations of the coding points are displayed in figures 19(a) and (b), which illustrate the cross-sections in the lateral and vertical focal plane views, respectively. Different colors indicate different coding points.

As illustrated in figure 19, a total of 35 coding points, comprising 280 points, were reconstructed in this experiment, achieving a reconstruction accuracy of 87.5%. Of these, 5 coding points were not successfully reconstructed because they could not be decoded due to occlusion during image acquisition, resulting in reconstruction failure. The above 3D reconstruction results of the coding points demonstrate that the methodology presented in this paper successfully achieves the 3D reconstruction of all unobstructed coding points on the focal plane and obtains the camera extrinsic matrix for all frames. This establishes a foundation for the subsequent 3D measurement of the fiber end face and baseline ruler.

4.4. Baseline ruler measurement

Given that the true value of the three-dimensional coordinates of the fiber end face is unknown, and the length of the baseline ruler is precisely measured with a measurement error of 0.001 mm, the measured value of the baseline ruler length can be considered as the true value. Based on this, we utilize absolute error and RMSE as evaluation metrics, calculate the length of the baseline ruler using the three-dimensional measurement method proposed in this paper, and design experiments to assess the measurement error of the method.

Table 4. Table of partial baseline ruler length measurements.

Baseline ruler code number	Gage length (mm)	Measuring length (mm)	Absolute error (mm)
1	38.700	38.684	0.016
2	39.490	39.505	0.015
3	78.190	78.188	0.002
4	908.020	907.926	0.093
5	988.050	988.136	0.086

Table 5. Results of ablation experiments against baseline scales.

Method	RMSE (mm)
Fixed threshold grayscale gravity method	0.075
Our adaptive threshold segmentation-based spot center extraction method	0.062
Adaptive weight filtering + adaptive segmentation-based extraction	0.049

The measurement results are presented in table 4, indicating that the minimum absolute error is 0.002 mm, the maximum absolute error is 0.093 mm, the mean absolute error is 0.038 mm, and the RMSE is 0.049 mm.

To assess our spot center extraction approach, we carried out a controlled ablation experiment, as presented in table 5. While maintaining all other processing steps invariant, we merely modified the center extraction method and employed the RMSE measured by the baseline ruler as the metric. Three configurations were tested: (1) Utilizing the conventional fixed-threshold gray centroid method for baseline measurement, resulting in an RMSE of 0.075; (2) Solely implementing our spot center extraction based on adaptive threshold segmentation, reducing the RMSE to 0.062; (3) Simultaneously applying adaptive weight filtering and extraction based on adaptive threshold segmentation, attaining the lowest RMSE value of 0.049.

As quantitatively demonstrated in table 5, each proposed technique contributes significantly to the reduction of errors, with the synergistic combination producing the optimal performance. These results not only confirm that our method achieves the lowest measurement error for baseline ruler measurement, but also provide direct evidence that the proposed techniques effectively reduce spot center extraction error. The progressive improvement observed through the stages of the ablation experiment conclusively validates the research approach developed in chapter 2.1.

Table 6. Table of fiber end-face 3D measurement results.

Number	X (mm)	Y (mm)	Z (mm)
1	210.451	345.532	558.737
2	210.530	318.045	558.250
3	186.873	331.574	559.408
4	517.280	332.380	525.508
5	493.758	317.517	524.701
6	513.350	302.905	524.087
7	400.242	235.162	541.998
8	367.724	226.484	542.630
9	396.742	201.529	541.786
10	529.374	107.010	480.033
11	536.243	93.900	478.043
12	518.015	83.100	479.393
13	215.390	106.672	543.839
14	201.827	82.060	545.425
15	254.462	85.600	544.479

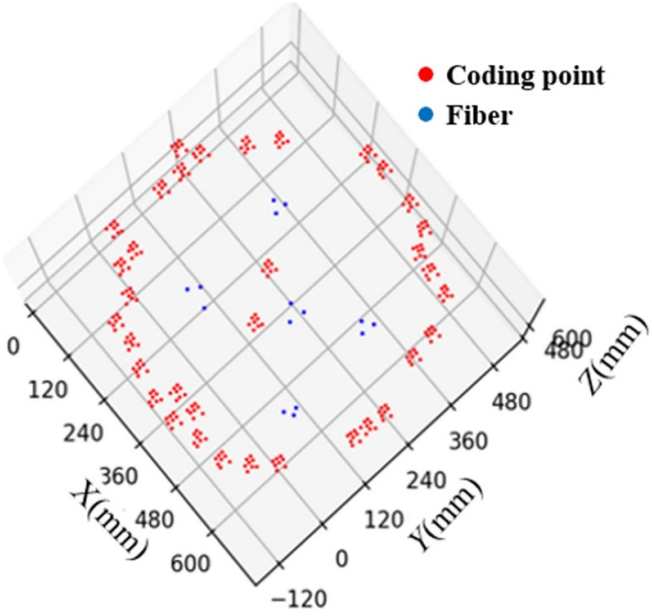

Figure 20. Visualisation of fiber 3D reconstruction.

4.5. Fiber end-face position measurement

After obtaining the global scale factor, we scale the overall 3D model, enabling the 3D measurement of the fiber end face position. The results are presented in table 6, along with the corresponding 3D visualization results of the coding points shown in figure 20.

To further validate the superiority of the 3D measurement method proposed in this paper and its contribution to efficiency improvement, we compare and analyze it with the traditional SFM method in terms of measurement error and efficiency. The key methods employed in various components are presented in table 7. In the measurement error assessment, we continue to use the RMSE of the baseline ruler measurement as the evaluation metric to compare the measurement error of the two methods. In the efficiency assessment, operational efficiency is evaluated based on the total time required to measure 15 fibers. The results are presented in table 7.

The experimental results presented in table 7 indicate that the SIFT-based feature extraction method exhibits a significant mis-matching issue, adversely affecting the accuracy of the camera's extrinsic matrix in the solution and hindering its ability to meet high accuracy requirements. In contrast, the coding point feature-based extraction and matching method focuses on specific points, effectively reducing mismatching and thereby improving the accuracy of the camera pose estimation. Additionally, it demonstrates strong computational efficiency, allowing for faster processing speeds in practical applications.

5. Conclusion

In response to the urgent demand for high-precision positioning of the fiber end face in the LAMOST closed-loop fiber positioning system, this paper proposes a three-dimensional measurement method for LAMOST fiber end faces under front and back illumination. This method addresses the errors associated with previous two-dimensional measurement techniques that approximated the curved focal plane of LAMOST as a flat surface. First, this paper analyzes the gray scale distribution characteristics of the acquired spot images and proposes an improved gray scale distribution spot center extraction method ES-GDM. This method accurately identifies and classifies the spots and extracts their centers, even in complex backgrounds. Compared to the traditional grayscale center of gravity method, ES-GDM reduces spot center extraction error by 34.7%. Next, to address the issue of insufficient texture features in fiber optic images that make matching difficult, we enhance the matching process by introducing coding information. Based on the design principles of coding points, we developed a DMCP-CPM strategy capable of fully automatic recognition and decoding of all coded spots across different fields of view, without the need for parameter settings. Finally we propose a 3D reconstruction method based on fused coding information SFM. This method gradually incorporates new viewpoint images to derive the camera poses corresponding to different frames, which are then used for the 3D reconstruction of all fiber end faces. Additionally, a rigorously measured baseline ruler was established on the focal plane to ensure the accurate physical scale of the recovered measurements. This baseline scale is incorporated into the reconstruction process to calculate the scale factor.

We developed the measurement system and conducted experimental validation at the National Astronomical Observatory of China. Qualitative experiments show that the 3D measurement methodology proposed in this paper achieves 3D reconstruction of 87.5% of the coding points and all fiber points on the focal plane, although some coding points cannot be reconstructed due to occlusions.

Table 7. Comparison table of key methods between traditional SFM and our method.

Method	Feature point extraction	Feature point matching	3D reconstruction	RMSE (mm)	Time (s)
Traditional SFM	SIFT	SIFT	Incremental SFM	1.232	98.685
Ours	ES-GDM	DMCP-CPM	Fusion-coded SFM	0.049	16.760

The quantitative experimental results indicate that the average absolute error for the baseline ruler 3D measurement is 0.049 mm, while its speed is improved compared to the traditional SfM method. The three-dimensional measurement method of focal plane fiber end-face position proposed in this paper is of great significance, and it can also provide a reference for the high-precision measurement of fiber end-face position in similar survey telescopes.

Data availability statement

The data cannot be made publicly available upon publication because they are owned by a third party and the terms of use prevent public distribution. The data that support the findings of this study are available upon reasonable request from the authors

Acknowledgment

Guoshoujing Telescope (the Large Sky Area Multi-Object Fiber Spectroscopic Telescope LAMOST) is a National Major Scientific Project built by the Chinese Academy of Sciences. Funding for the project has been provided by the National Development and Reform Commission. LAMOST is operated and managed by the National Astronomical Observatories, Chinese Academy of Sciences.

ORCID iDs

Rui Wang https://orcid.org/0000-0002-4813-8514
Shijie Li https://orcid.org/0009-0003-8331-096X
Jian Zhou https://orcid.org/0009-0000-5794-2371
Junhua Sun https://orcid.org/0000-0002-9707-9194

References

Bay H, Ess A, Tuytelaars T and Van Gool L 2008 Speeded-Up Robust Features (SURF) *Comput. Vis. Image Underst.* **110** 346–59
Bernardini G, Serafini J, Enei C, Mattioni L, Ficuciello C and Vezzari V 2016 Structural characterization of rotor blades through photogrammetry *Meas. Sci. Technol.* **27** 065401
Cui X-Q *et al* 2012 The Large Sky Area Multi-Object Fiber Spectroscopic Telescope (LAMOST) *Res. Astron. Astrophys.* **12** 1197
Ester M *et al* 1996 A density-based algorithm for discovering clusters in large spatial databases with noise *KDD'96: Proc. of the Second Int. Conf. on Knowledge Discovery and Data Mining* (*Portland, Oregon*) pp 226–31
Fisher C *et al* 2014 Developing engineering model Cobra fiber positioners for the Subaru Telescope's prime focus spectrometer *Proc. SPIE* **9151** 661–73
Gavaskar R G and Chaudhury K N 2018 Fast adaptive bilateral filtering *IEEE Trans. Image Process.* **28** 779–90
Gu Y, Zhai C, Xing X and Chu J 2008 A new method for measuring the position of the end of optical fibers for LAMOST *Proc. SPIE* **7014** 1430–8
Hartley R 2003 *Multiple View Geometry in Computer Vision* vol 665 (Cambridge University Press)
Le T M, Fatahi B, Khabbaz H and Sun W 2017 Numerical optimization applying trust-region reflective least squares algorithm with constraints to optimize the non-linear creep parameters of soft soil *Appl. Math. Modelling* **41** 236–56
Li W *et al* 2004 The measurement system for fiber positioning unit of LAMOST *Proc. SPIE* **5492** pp 584–91
Lowe D G 1999 Object recognition from local scale-invariant features *Proc. 7th IEEE Int. Conf. on Computer Vision* vol 2 (IEEE) pp 1150–7
MacQueen J *et al* 1967 Some methods for classification and analysis of multivariate observations *Proc. 5th Berkeley Symp. on Mathematical Statistics and Probability* vol 1 pp 281–97
Montgomery D *et al* 2016 Development of the fibre positioning unit of MOONS *Proc. SPIE* **9908** 2734–48
Pan Z *et al* 2022 Closed-loop control system based on visual measurement for LAMOST optical fiber positioning *Proc. SPIE* **12166** 1023–29
Schonberger J L and Frahm J-M 2016 Structure-from-motion revisited *Proc. IEEE Conf. on Computer Vision and Pattern Recognition* pp 4104–13
Schubnell M *et al* 2016 The DESI fiber positioner system *Proc. SPIE* **9908** 2715–20
Shapiro R 1978 Direct linear transformation method for three-dimensional cinematography *Res. Q. Am. Alliance Health Phys. Educ. Rec.* **49** 197–205
Sun J and Xie Y 2023 Subpixel spot localization using multiscale anisotropic Gaussian tensor *Measurement* **214** 112756
Wang S-Y *et al* 2012 The metrology cameras for Subaru PFS and FMOS *Proc. SPIE* **8446** 84464Z
Watson S *et al* 2022 MOONS fibre positioning module: instrument build overview *Proc. SPIE* **12188** 1218829
Winkler R *et al* 2022 4MOST metrology system lab calibration and performance *Proc. SPIE* **12188** 121882A
Winkler R, Barden S C and Saviauk A 2016 4MOST metrology system image processing *Proc. SPIE* **9908** 990891
Xing X, Hu H and Chu J 2007 Optical fiber positioning technology for LAMOST *J. Univ. Sci. Technol. China* **37** 596–600
Yang J, Wei H, Li L, Feng Y, Hu Y and Wang L 2024 A new target color adaptive graying and segmentation method for gear contact spot detection *Meas. Sci. Technol.* **36** 015424
Zhao K *et al* 2018 The improvement of LAMOST fiber view camera metrology system fiber position recognition algorithm *Proc. SPIE* **10702** 1070277
Zheng B, Dong Y, Mullany B, Morse E and Davies A 2013 Positioning sensor by combining photogrammetry, optical projection and a virtual camera model *Meas. Sci. Technol.* **24** 105106
Zhou L, Luo Y and Zhang L 2024 Fast inspection of flange faces of welded tubes using photogrammetry and auxiliary measuring tools *Measurement* **237** 115256